K-1 Coupled GCM (MIROC) Description

K-1 model developers
Center for Climate System Research (CCSR), University of Tokyo; National Institute for Environmental Studies (NIES); Frontier Research Center for Global Change (FRCGC)

Edited by Hiroyasu Hasumi and Seita Emori

September, 2004

K-1 model developers (in alphabetical order):

ABE-OUCHI, Ayako (CCSR/FRCGC)
EMORI, Seita (NIES/FRCGC)
HASEGAWA, Akira (FRCGC)
HASUMI, Hiroyasu (CCSR)
INOUE, Takahiro (Research Organization for Information Science and Technology)
KIMOTO, Masahide (CCSR)
MATSUMURA, Shinji (FRCGC)
NAGASHIMA, Tatsuya (NIES)
NAKANO, Hideyuki (CCSR, currently at Meteorological Research Institute)
NISHIMURA, Teruyuki (FRCGC)
NOZAWA, Toru (NIES)
OHGAITO, Rumi (FRCGC)
OKA, Akira (CCSR)
OKADA, Naosuke (NIES)
OGOCHI, Koji (NEC Solutions)
OGURA, Tomoo (NIES)
SAITO, Fuyuki (CCSR)
SAITO, Kazuyuki (FRCGC)
SAKAMOTO, Takashi (FRCGC)
SEGAWA, Tomonori (FRCGC)
SOGA, Takashi (NEC Solutions)
SUDO, Kengo (FRCGC)
SUMI, Akimasa (CCSR)
SUZUKI, Tatsuo (FRCGC)
SUZUKI, Tsuneaki (FRCGC)
TAKAHASHI, Hideki (NEC Solutions)
TAKATA, Kumiko (FRCGC)
TAKEMURA, Toshihiko (Kyushu University)
TAKIGAWA, Masayuki (FRCGC)
TSUSHIMA, Yoko (FRCGC)
WATANABE, Masahiro (Hokkaido University)
WATANABE, Shingo (FRCGC)
YOKOHATA, Tokuta (NIES)

Corresponding to:
Hiroyasu Hasumi
Center for Climate System Research, University of Tokyo
4-6-1 Komaba, Meguro-ku, Tokyo 153-8904, Japan
E-mail: hasumi@ccsr.u-tokyo.ac.jp

Contents

1 Overview: Structure of MIROC

The Model for Interdisciplinary Research on Climate (MIROC), which is the coupled general circulation model used in the K-1 project, consists of five componet models: atmosphere, land, river, sea ice, and ocean. The atmospheric component interacts with the land and sea ice components. The air-sea exchange is realized exclusively between the atmosphere and sea ice components, not directly between the atmosphere and ocean components, and the ocean component interacts only with the sea ice component. That is, air-sea flux at ice-free grids is consequently passed to the ocean component without modification, but it is first passed to the sea ice component. The river component receives ground runoff water from the land component and drains riverine runoff water into the sea ice component. Lakes are dealt with by the sea ice and ocean components.

Two MIROC setups of different resolution are used in the K-1 project and are described herein. The higher resolution setup is referred to as "HI" and the lower resolution one as "MID" hereafter.

1.1 Flux coupler

Model resolution and grid system are independently chosen for each component, and time integration also proceeds independently. Note that the sea ice and ocean components share the same horizontal resolution and grid system, and their time integration is synchronized. The fluxes of heat, water, and momentum and the physical quantities necessary for the flux calculation (surface air temperature for the air-sea heat flux calculation in the sea ice component, for example) are passed from one component to another with a prescribed time interval. The exchaged fluxes are stocked in the "coupler" and time-averaged over that interval, while the latest values are passed at the timing of exchange for the other referenced variables. The sea ice and ocean components use the same time step, and the exchange is realized at every time step.

The coupler grid system is generated by dividing each atmospheric grid by meridians and latitude circles, as the resolution of the land and sea ice components is no lower than that of the atmospheric component in usual applications. The atmospheric variables necessary for the surface flux calculation are interpolated onto the coupler grid system. As for the fluxes calculated in the atmospheric component and passed to the land or sea ice component (precipitation, for example), the same flux value is assigned to each of the corresponding coupler grids. The atmosphere-sea ice coupler grid system is also used for the river-sea ice exchange, and the atmosphere-land coupler grid system is also used for the land-river

exchange.

Atmosphere-land coupling   The atmosphere-land coupler grid system always coincides with the land component grid system, so the land surface fluxes calculated in the land compoent model at each grid are simply passed to the atmosphere-land coupler grids, and each atmospheric grid takes up the fluxes averaged over the corresponding coupler grids. The number of division for the coupler grid generation is two in both zonal and meridional for HI, and is one for MID.

Atmosphere-sea ice coupling   The atmosphere-sea ice coupler grid system does not necessarily coincides with the sea ice component grid system. Each coupler grid generally covers more than one sea ice component grid, some of which partially and others entirely. For each coupler grid, therefore, covered sea ice grids and their fractional areal coverage are tabulated beforehand. Likewise, covered coupler grids and their fractional areal coverage are tabulated for each sea ice model grid. The fluxes and variables are converted between the coupler grid system and the sea ice model grid system by using these tables and areal weights. Fluxes are exchaged without any leak through this procedure. The number of division for the coupler grid generation is four in zonal and six in meridional for HI, and is two both in zonal and meridional for MID.

Land-river-sea ice coupling   The river component receives ground runoff water from the atmosphere-land coupler and passes riverine runoff water to the atmosphere-sea ice coupler. The river component model grid system is generally different from either of the two coupler grid systems, so ground runoff water from more than one atmosphere-land coupler grid is passed to a single river grid, and riverine runoff water from more than one river grid is passed to a single atmosphere-sea ice coupler grid. The conversion between the grid systems is achived by a method similar to the case of the air-sea exchange, and the total water is conserved through this procedure.

Coastal boundary   The coastal boundary is defined by the sea ice component grid system and can be chosen independently of the atmospheric component's resolution and grid system. Therefore, land and sea can co-exist in a single atmospheric model grid. Area of coastal land grids is adjusted so that the sum of the land area and the sea area covered by a single atmospheric model grid becomes the same as the area of that atmospheric grid.

Coupling interval The coupling interval of HI is 3 hours for all the exchanges. The inteveral for MID is 3 hours for the exchange between sea ice and others, and is 20 minutes for the other exchanges.

1.2   Coupling strategy for parallel computing

The multi-program multi-data (MPMD) method is used for parallel computing, where the component models are divided into two parts, the atmosphere-land-river part and the sea ice-ocean part, and these two parts run in parallel on different groups of processors. It means that the coupled model is divided at the atmosphere-sea ice coupler. Necessary data are exchanged between the two parts at the timing of the atmosphere-sea ice coupling. The number of processors for each part is so chosen that the computational time required for the integration over a given period becomes the same between the two parts.

2 Atmospheric model

The atmospheric general circulation model used herein is the CCSR/NIES/FRCGC AGCM version 5.7, which is based on the CCSR/NIES AGCM described in Numaguti et al. (1997; hereafter, N97). Here, only the outline of the model along with the modifications done after N97 was written are described.

2.1 General features

The dynamical part of the CCSR/NIES/FRCGC AGCM solves the primitive equations on a sphere using a spectral transform method. The vertical coordinate used in this particular version is σ (pressure normalized by surface pressure), while σ-pressure hybrid coordinate has also been implemented in the model. For the advection of tracers, a finite difference scheme with the piecewise parabolic method (PPM) is used in conjunction with the flux form semi-Lagrangian scheme (Lin and Rood, 1996), which is a new feature not having appeared in N97 and will be described in Subsection 2.5.

The prognostic variables are zonal and meridional velocity, temperature, surface pressure and mixing ratios of arbitrary number of tracers including water vapor (specific humidity) and cloud liquid water. When the interactive aerosol module (sSPRINTARS, a simplified version of SPRINTARS: Spectral Radiation-Transport Model for Aerosol Species; Takemura et al., 2000, 2002) is activated, several aerosol species are also included in the tracers. In addition, cloud base mass flux of cumulus convection is also prognosed in this particular version.

The physical parameterizations included are a radiation scheme with two-stream k-distribution method, a prognostic Arakawa-Schubert cumulus scheme, a prognostic cloud water scheme for large-scale condensation, a turbulence closure scheme with cloud effect, and an orographic gravity wave drag scheme. What is remarkably new in the physical parameterizations is the treatment of direct and indirect radiative effects of aerosols. The direct effect and the first indirect (cloud albedo) effect is treated in the radiation scheme, while the second indirect (cloud lifetime) effect in the large-scale condensation scheme. Those will be described in Subsections 2.6 and 2.7.

2.2 Discretization and resolution

The spatial discretization method used are a spectral transformation method with Gaussian grid in horizontal and a grid differentiation (Arakawa and Suarez, 1983) in vertical.

For the temporal discretization, a leap-frog scheme is basically used. The integration are divided into two steps: the dynamics step treating adiabatic advective processes in resolvable scale and the physics step treating the other processes. The time step is variable depending on maximum wind speed to meet the CFL condition.

In the higher-resolution setup (HI), the horizontal resolution is T106 spectral truncation, which is approximately equivalent to 1.125° longitude-latitude grid. The model has 56 vertical σ layers with relatively finer vertical resolution in the planetary boundary layer and around the tropopause. The σ values of the vertical layer boundarys (half-levels) are: 1.000, 0.995, 0.988, 0.978, 0.966, 0.951, 0.933, 0.912, 0.889, 0.863, 0.835, 0.805, 0.769, 0.725, 0.673, 0.6130, 0.5510, 0.4880, 0.4330, 0.3920, 0.3580, 0.3290, 0.3030, 0.2800, 0.2590, 0.2400, 0.2220, 0.2050, 0.1890, 0.1750, 0.1620, 0.1500, 0.1380, 0.1280, 0.1180, 0.1090, 0.1010, 0.0933, 0.0863, 0.0798, 0.0737, 0.0682, 0.0630, 0.0578, 0.0523, 0.0467, 0.0410, 0.0356, 0.0300, 0.0242, 0.0187, 0.0139, 0.0097, 0.0063, 0.0038, 0.0022 and 0.0000. The height of the model top is approximately 40km.

In the lower-resolution setup (MID), the horizontal resolution is T42, approximately equivalent to 2.8125°. The model has 20 vertical σ layers with relatively finer vertical resolution in the planetary boundary layer. The σ values of the vertical layer boundarys (half-levels) are: 1.000, 0.990, 0.970, 0.930, 0.870, 0.790, 0.700, 0.600, 0.500, 0.410, 0.330, 0.260, 0.200, 0.150, 0.100, 0.070, 0.050, 0.040, 0.030, 0.020 and 0.0001. The height of the model top is approximately 30km.

Related to the difference in horizontal and vertical resolution and the model top height, different strength of horizontal diffusion is specified in HI and MID. The e-folding time scale for the horizontal diffusion is 6 hours in HI and 24 hours in MID, while stronger diffusion is applied in the top 4 layers in HI.

2.3   Physical parameterizations

Each of the physical parameterizations adopted are described below in the order in which they are applied in the model. The prognostic variables are updated three times in each physics step due to the adjustment-like nature of moist processes: the first is after cumulus convection, the second after large-scale condensation, and the third is at the end of the physics step.

Cumulus convection   The cumulus parameterization scheme is based on Arakawa and Schubert (1974) with several simplifications described in N97. The closure assumption is

changed from the diagnostic closure used in N97 to a prognostic closure based on Pan and Randall (1998), in which cloud base mass flux is treated as a prognostic variable. An empirical cumulus suppression condition introduced in Emori et al. (2001) is adopted. Cumulus convection is suppressed when cloud-mean ambient relative humidity is less than a certain critical value, which is set to 0.8 in the present version. The momentum transport by cumulus convection based on Gregory et al. (1997) has been implemented and is activated only in MID. Since this scheme seems to hinder the organization of tropical precipitation in HI, it is temporary suppressed in HI. Other modifications include: an improved downdraft treatment in which saturated downdraft is more properly represented, gradual melting of precipitation to avoid too strong temperature kink at melting levels, and a column-based a posteriori water mass fixer to remove negative humidity.

Large-scale condensation   The large-scale condensation scheme describes grid-scale condensation and precipitation processes and gives condensational heating, precipitation, cloud fraction and change of water vapor and cloud liquid water. The scheme has been developed based on the scheme of Le Treut and Li (1991), in which subgrid probability distribution of total water mixing ratio in each grid box is assumed as a uniform distribution. The range of the uniform distribution was prescribed as a function of height in the version described in N97 (not explicitly written in N97). In the present version, the range is enhanced where detrainment of cumulus convection occurs for an efficient formation of anvil clouds. The phase of cloud (solid or liquid) is diagnosed according to temperature, T. That is, the ratio of liquid cloud water to total cloud water, f_{liq}, is given by:

$$f_{liq} = \min(\max((T - T_w)/(T_s - T_w), 0), 1),$$

where T_s and T_w are set to 273.15 K and 258.15 K, respectively, in the present version. However, this diagnosis should be applied only to locally condensed cloud. The fallen ice cloud should be continued to be treated as ice, and treated as rainfall when it melts. To try to distinguish the locally condensed cloud and the fallen ice, it is assumed that the ratio of the former to the total is proportional to the generation tendency of the former to that of the total. The second indirect effect of aerosols (cloud lifetime effect) is also represented, which will be described in a separated subsection (Subsection 2.6). Two uncertain parameters primarily used for callibration of the top-of-the-atmosphere radiation budget of the atmospheric model (when realistic SST is prescribed) reside in this part. They are 'vice0' and 'b1', and respectively related to ice fall velocity and auto-conversion time scale of liquid precipitation. In HI and MID, different values are specified for these two parameters.

Radiative transfer   The radiative transfer scheme employed is based on the two-stream discrete ordinate method and the k-distribution method. The basic description of the original radiation code of CCSR/NIES/FRCGC AGCM (hereafter MSTRN) is written in Nakajima et al. (2000). In the present version, the total number of bands (channels) is 18(37), 11(30) for IR and 7(7) for visible-UV. The number of the band tuned by k-distribution is 13. The treatments of clouds and aerosols have been improved since Nakajima et al. (2000) was written especially related to the direct and indirect effects of aerosols. Those will be described in a separated subsection (Subsection 2.7).

Surface flux   The calculation of surface fluxes, including turbulent fluxes of momentum, sensible and latent heat, and short-wave and long-wave radiative fluxes, has been separated from the atmospheric model. The atmospheric model receives those fluxes from the ocean model and the land-surface model through a flux-coupler and uses them as lower boundary conditions of vertical diffusion and radiative transfer.

Vertical diffusion   The level 2 scheme of turbulence closure model by Mellor and Yamada (1974, 1982) is used for the subgrid vertical fluxes of prognostic variables. The effect of free convection described in N97 has been removed. The treatment of cloud effect for the turbulent flux is changed from that described in N97 to one based on Smith (1990). In the new scheme, the thermodynamic variables to be transported by turbulence are total water and liquid water potential temperature, instead of water vapor and potential temperature as in the old scheme. After the vertical diffusion is calculated, cloud water, water vapor and temperature are diagnosed in a manner consistent with the large-scale condensation scheme. A non-local turbulence closure scheme based on Holtslag and Boville (1993) has also been implemented and can be used in conjunction with the Mellor-Yamada level 2, but not activated in the present version.

Internal gravity wave drag   The effects of orographically exited subgrid scale internal gravity wave is parameterized following McFarlane (1987). No modification has been made over N97. The strength of this drag is obviously resolution dependent. Different parameter values are used in HI and MID.

2.4   Boundary conditions

The lower boundary conditions required are surface height and the standard deviation of the surface height over each grid box, which are generated from the USGS GTOPO30 dataset.

The three dimensional (or zonal-mean) distribution of ozone concentration is also required. When the interactive aerosol module is not activated, the three dimensional distributions of mass concentration of various aerosol species and number concentration of total aerosol available for cloud condensation nuclei should be prescribed, while various emission data is required when the aerosol module is activated.

2.5 Tracer advection

The conservation law in flux form   The flux form of the conservation law for a conservative scalar q in multi–dimensional coordinates is expressed as eq.(2.2) in Lin and Rood (1996; hereafter LR96). Discretizing by $x = x_i$ ($i = 1, 2, 3..$), $y = y_j$ ($j = 1, 2, 3..$), and $\sigma = \sigma_k$ ($k = 1, 2, 3..$), eq.(2.2) in LR96 can be rewritten as

$$
\frac{\partial P^S q_{i,j,k}}{\partial t} = \frac{1}{\Delta x_{i,j,k}}(F^x_{i-\frac{1}{2},j,k} - F^x_{i+\frac{1}{2},j,k})
$$
$$
+ \frac{1}{\Delta y_{i,j,k}}(F^y_{i,j-\frac{1}{2},k} - F^y_{i,j+\frac{1}{2},k})
$$
$$
+ \frac{1}{\Delta \sigma_{i,j,k}}(F^\sigma_{i,j,k-\frac{1}{2}} - F^\sigma_{i,j,k+\frac{1}{2}}). \tag{1}
$$

Here, P^S denotes the surface pressure, $F^x_{i-\frac{1}{2},j,k}$ denotes the mass flux of tracer constituents for the x–direction on the boundary between cell (i, j, k) and cell $(i-1, j, k)$ (cf. Fig.1 in LR96), and $\Delta x_{i,j,k}$ denotes the width of cell (i, j, k) for the x–direction. The total constituent mass (global integral of constituent density) is generally conserved in an operator–split flux–form scheme without a posteriori restoration. The precision and characteristics (*e.g.,* stability and monotonicity) of this advection scheme depends on the selection of computational scheme for the calculation of mass transfer across the cell ($F^x_{i-\frac{1}{2},j,k}$). CCSR/NIES/FRCGC AGCM can choose between two types of van Leer–type schemes for the calculation of $F^x_{i-\frac{1}{2},j,k}$, by considering computational cost and the precision. One is the 4th–order monotonic van Leer scheme (called as FFSL–2 in LR96) and the other is the Piecewise Parabolic Method (PPM) scheme with monotonic constraint (FFSL–3 in LR96). Lin et al. (1994) describes general formulation of the 4th–order monotonic van Leer scheme, and Carpenter et al. (1990) and Colella and Woodward (1984) describe general formulation of the PPM scheme. The monotonicity constraint for the PPM scheme is described in Appendix C of LR96. Each of these schemes

1. compute fluxes based on the sub-grid distribution in the upwind direction

2. generate no new maxima or minima (*i.e.,* monotonicity is satisfied)

3. generate no negative value

4. are stable when the Courant number in each direction is less than 1.

The PPM scheme needs more computational cost compared to the 4th–order van Leer scheme, but it can calculate $F^x_{i-\frac{1}{2},j,k}$ with less computational dissipation. Therefore, the PPM scheme is applied for the k–1 coupled–model calculation.

Application to a spectral model For the calculation of the time–averaged mass flux across the cell boundary, the winds and the tracer distributions are staggered in the Arakawa C–grid (cf., Mesinger and Arakawa, 1976). The horizontal winds at the cell boundary, $u_{i-\frac{1}{2},j,k}$ and $v_{i,j-\frac{1}{2},k}$, are reconstructed by using the mass convergence field in the spectral model and the discretized continuity equation:

$$\frac{\partial P^S_{i,j,k}}{\partial t} = \frac{1}{\Delta D_{j,k}}\{(V^\lambda_{i-\frac{1}{2},j,k} - V^\lambda_{i+\frac{1}{2},j,k}) + (V^\varphi_{i,j-\frac{1}{2},k} - V^\varphi_{i,j+\frac{1}{2},k}) + (V^\sigma_{i,j,k-\frac{1}{2}} - V^\sigma_{i,j,k+\frac{1}{2}})\}. \qquad (2)$$

Here, $V^\lambda_{i-\frac{1}{2},j,k}$, $V^\varphi_{i,j-\frac{1}{2},k}$, and $V^\sigma_{i,j,k-\frac{1}{2}}$ denote zonal, meridional, and vertical mass–weighted wind at the cell boundary, respectively. That is,

$$V^\lambda_{i-\frac{1}{2},j,k} = (P^S u)_{i-\frac{1}{2},j,k}\Delta y_j \Delta\sigma_k \qquad (3)$$

$$V^\varphi_{i,j-\frac{1}{2},k} = (P^S v)_{i,j-\frac{1}{2},k}\Delta x_{j-\frac{1}{2}} \Delta\sigma_k \qquad (4)$$

$$V^\sigma_{i,j,k-\frac{1}{2}} = (P^S \dot\sigma)_{i,j,k-\frac{1}{2}}\Delta x_j \Delta y_j. \qquad (5)$$

$\Delta D_{j,k}$ denotes the cell volume, and Δx_j, Δy_j, and $\Delta\sigma_k$ denote zonal, meridional, vertical width of the cell, respectively. That is, $\Delta D_{j,k} = a\cos\varphi_j \Delta\lambda\Delta\varphi_j\Delta\sigma$, $\Delta x_j = a\cos\varphi_j\Delta\lambda$, and $\Delta y_j = a\Delta\varphi_j$.

The following are the procedure for the calculation of tracer advection in the staggering–grided horizontal and vertical wind fields:

1. Surface pressure P^S and horizontal wind $\boldsymbol{v}$ at time step $t + \Delta t$ are predicted in the spectral model.

2. The horizontal component of mass flux divergence at time step t is calculated by using spherical harmonics. The mass fluxes at time step t are reconstructed from the values at $t + \Delta t$ and $t - \Delta t$, because CCSR/NIES AGCM applies semi–implicit scheme for the time–integration of surface pressure. Zonal and meridional component of mass flux divergence are:

$$C^x = -\frac{1}{a\cos\varphi}\frac{\partial}{\partial\lambda}(P^S u), \quad C^y = -\frac{1}{a\cos\varphi}\frac{\partial}{\partial\varphi}(P^S v\cos\varphi).$$

9

3. By applying C_x and C_y into eq.(3) and eq.(4), V^λ, V^φ are calculated by using:

$$V^\lambda_{i-\frac{1}{2},j,k} - V^\lambda_{i+\frac{1}{2},j,k} = C^x_{i,j,k}\Delta D_{j,k} \tag{6}$$

$$V^\varphi_{i,j-\frac{1}{2},k} - V^\varphi_{i,j+\frac{1}{2},k} = C^y_{i,j,k}\Delta D_{j,k}. \tag{7}$$

The boundary conditions for eq.(6) and eq.(7) are $V^\varphi = 0$ at the North Pole and the South Pole, and zonal average of V^λ is equal to that in the spectral model grid.

By integrating eq.(2) from the top to the bottom of the vertical σ domain,

$$\frac{\partial P^S_{i,j,k}}{\partial t}\sum_k \Delta D_{j,k} = \sum_k (C^x_{i,j,k} + C^x_{i,j,k}). \tag{8}$$

V^σ is calculated from eq.(2) and eq.(8), with the boundary condition of $V^\sigma = 0$ at the surface and the top of the atmosphere.

4. The mass flux for tracer constituents F^x, F^y, and F^σ are calculated by using van Leer–type scheme (4th order monotonic van Leer scheme or monotonic PPM scheme) from the mass–weighted winds V^λ, V^φ, and V^σ. If the absolute value of the Courant number exceeds 1, a Flux–form semi–Lagrangian (FFSL) treatment is applied, *i.e.*, the mass flux is separately calculated as the integer flux and the fractional flux, following to LR96. Since the meridional and vertical flux are negligibly small compared to the zonal flux, FFSL treatment is considered only for F^x at present.

5. $P^S q$ at time step $t + \Delta t$ is calculated from eq.(1). $q_{t+\Delta t}$ can be obtained by dividing $(P^S q)_{t+\Delta t}$ by the surface pressure at time step $t+\Delta t$. There is small quantity of difference between $P^S_{t+\Delta t}$ from eq.(8) and $P^S_{t+\Delta t}$ in the spectral model, because CCSR/NIES AGCM applies the semi–implicit time integration scheme. $P^S_{t+\Delta t}$ from eq.(8) is applied at present for the consistency of mass advection. Mass conservation is not strictly satisfied because of the discrepancy between the surface pressure in the spectral model and $P^S_{t+\Delta t}$ from eq.(8).

The mass fluxes into/out of polar caps   The mass fluxes into/out of polar caps are calculated by using the semi–Lagrangian scheme in the polar stereo projection (cf. Figure 2.5). The horizontal average at the highest latitude band is assumed to be preserved before/after flux calculation for the mass conservation. The sequence of calculation is:

1. Zonal average of $P^S q$ at time step t is calculated at the highest latitude band, and is assumed to equal $P^S q$ at the pole.

10
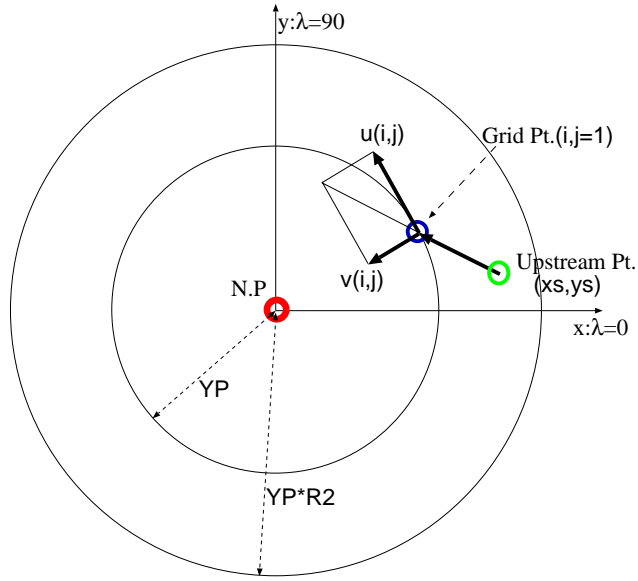
Figure 1: Conceptual figure for the flux on pole-most grids.

2. Horizontal wind at the highest latitude bands is projected into the orthogonal coordinate system centering around the pole, and q at time step $t + \Delta t$ is estimated by using the value at the "departure point".

3. Zonal average of $(P^S q)_{t+\Delta t}$ is fixed to that of $(P^S q)_t$.

2.6 Aerosol indirect effects in large-scale condensation

The present version considers both the first and second aerosol indirect effects only for stratus water cloud. The cloud droplet number concentration N_c is diagnosed referring to the observation by Martin et al. (1994):

$$N_c = \frac{\epsilon N_a N_m}{\epsilon N_a + N_m},$$

where N_a is the aerosol particle number concentration excluding soil dust and black carbon, and ϵ and N_m are constants. The monthly mean data of the three-dimensional aerosol number concentration used here is prescribed off-line by SPRINTARS, or they are calculated on-line at each time step when the interactive aerosol module is activated. If the function of the cloud droplet size distribution is fixed, its effective radius r_{eff} is decided as follows:

$$r_{eff} = k \left(\frac{3}{4\pi \rho_w} \frac{\rho l}{N_c} \right)^{\frac{1}{3}},$$

where ρ is the air density, l is the cloud water mixing ratio, ρ_w is the water density, and k is an empirical constant. The Berry's parameterization is adapted to the precipitation rate P, which depends on not only l but also N_c (Berry, 1967):

$$P = -\frac{dl}{dt} = \frac{\alpha \rho l^2}{\beta + \gamma \frac{N_c}{\rho l}},$$

where t is time and α, β, and γ are constants.

2.7 Cloud and aerosol treatments in radiation scheme

The optical parameters for seven species of particulate matter, two types of cloud (water cloud and ice cloud) and five aerosol species (soil dust, black carbon (BC), organic carbon (OC), sulfate, and sea salt) are included. The classification of aerosols is based on SPRINT-ARS (Takemura et al., 2000, 2002). The parameters are calculated off-line, and the GCM access them through a table.

Aerosol microphysics and its radiative effect on water cloud As mentioned in the Subsection 2.6, the radius of water cloud varies depending on the aerosol particle number concentration. The monthly mean data of the three-dimensional aerosol mass and number concentrations used in the radiative process are prescribed off-line by SPRINTARS, or they are calculated on-line at each time step when the interactive aerosol module is activated.

The hygroscopic growth of aerosols is expressed according to Tang and Munkelwitz (1994) for sulfate and Hobbs et al. (1997) for OC, and they are assumed to be homogeneously intermingled with water. The relationship between the relative humidity and its volume mode radius is shown in Table 1.

Table 1: volume mode radius r_g of OC and sulfate depending on relative humidity (RH).

RH (%)	0	50	70	80	90	95	98	99
$r_g(\mu m)$ (OC)	0.237	0.256	0.261	0.342	0.401	0.456	0.650	0.740
$r_g(\mu m)$ (sulfate)	0.243	0.298	0.333	0.361	0.427	0.550	0.683	0.809

Optical parameters for clouds and aerosols The refractive indices of water and dry aerosols used in preparing the optical parameter table are according to d'Almeida et al. (1991) and WCP-55 (1983), but their imaginary part of soil dust at visible wavelength is one-fourth of WCP-55 (1983) in this model, which is fitted to recent observations. The

coefficients of extinction and absorption and the first five orders of Legendre moments of the volume scattering phase function in each wavelength band are written in the table. We assume that the shape of the particulate matters spherical. The distribution of particle radii is calculated assuming a lognormal distribution and taking the values shown in Table 2 as the volume mode radius and standard deviation of the distribution. The optical parameters are calculated for the eight sizes of volume mode radius for each species of particulate matter. For the hygroscopic aerosols (OC and sulfate aerosols), the optical parameters are calculated for eight radii in accordance with the relative humidity taking account of hygroscopic particle growth as described in the previous section (Table 1), and then they are interpolated depending on the relative humidity in each model grid. The effect of the particle size on the radiative flux is expressed by the interpolation of the moments of the volume scattering phase function of the referenced volume mode radius in the table.

Table 2: volume mode radius r_g and standard deviation σ for each particulate matter. *see Table 1.

	water cloud	ice cloud	soil dust	BC	OC	sulfate	sea salt
$r_g(\mu m)$	variable	40.0	4.00	0.0390	variable*	variable*	2.00
σ	1.5	1.5	2.5	2.0	1.8	2.0	2.5

Vertical cloud overlapping   In the original MSTRN, the semi-random method was used to treat cloud overlap (Nakajima et al.,2000). While this computationally efficient method works well for an AGCM, the appropriateness of random overlap assumption depends on vertical resolution of the model.

This is because, in the random overlap assumption, the ratio of cloud overlapping increases as the number of vertical layers increases. When a mass of cloud exist in the continuous layers, it is not reasonable. When the model resolves a cloud, the adjacent layers which contain cloud should be treated assuming maximum overlap.

Several different algorithms have been proposed which compute the maximum-random overlap assumption, in which adjacent cloud layers overlap maximally and discrete cloud layers are independent. We adopted the method of Geleyn and Hollingsworth (1979, hereafter GH). This method allots the radiative fluxes to clear and cloudy segments according to the ratio of the cloud fractions in adjacent layers. As a result, the radiative fluxes are obtained under the condition of maximum-random overlap. Since we calculate the multiple scattering of light between model layers by the adding method (Nakajima et al., 2000), we cannot apply

13

the original GH method to MSTRN directly; therefore we re-formulated the GH method. The new formulation is mathematically equivalent to the original, and is similar to that of the four-stream approximation (Shibata and Uchiyama, 1992).

3 Land-surface model

The land-surface model used herein is MATSIRO (Minimal Advanced Treatments of Surface Interaction and RunOff), which is described in Takata et al. (2003).

3.1 General features

MATSIRO represents energy and water exchange between land-surface and atmosphere. MATSIRO receives temperature, specific humidity, wind speed, and pressure of the lowest atmospheric layer, and precipitation and downward short-wave and long-wave radiation fluxes from the atmospheric model, while it provides turbulent fluxes of momentum, sensible and latent heat, and upward short-wave and long-wave radiation fluxes to the atmospheric model. It also provides runoff flux to the river routing model. The prognostic variables of MATSIRO are canopy temperature and surface temperature of snow-free and snow-covered areas, canopy water content, snow amount, snow temperature, snow albedo, soil temperature, soil moisture content, and frozen soil moisture content.

3.2 Model structure and resolution

The model consists of two parts: flux part and integration part. The flux part is invoked by the atmospheric model in each time step of the atmospheric model. It provides fluxes to the atmosphere and updates canopy and surface temperature. The integration part updates canopy water content and snow and soil variables. Its time step is 3 hours.

The model has 1 canopy layer, 5 soil layers, and variable number of snow layers (0–3 depending on the snow amount). The thickness of the soil layers from the top are: 5cm, 20cm, 75cm, 100cm and 200cm. Canopy and surface skin layer do not have heat capacity.

In HI, the horizontal grid structure of the model is 2×2 tiling of each atmospheric model grid box, that is, the resolution is approximately 0.5625° in longitude and latitude. In MID, the horizontal resolution and the grid structure are the same as those of the atmospheric model, that is, T42 ($\sim$2.8125°).

3.3 Processes treated

Surface flux   The turbulent fluxes from canopy and surface are calculated based on Watanabe (1994). The fluxes over snow-free and snow-covered areas are calculated separately and averaged afterward weighted with area fractions. The stomatal conductance is evaluated on the basis of a photosynthesis-stomatal conductance model (e.g., Farquhar et al., 1980; Ball

15

1998).

Canopy water The canopy water content is determined by the balance of canopy interception of precipitation, canopy evaporation and dripping.

Snow The snow amount is determined by the balance of snow fall, snow melt and sublimation. The snow temperature is calculated by a heat conduction equation. The snow albedo calculation is based on Wiscombe and Warren (1980).

Runoff The TOP model approach (Beven and Kirkby, 1979) is adopted with simplification. Saturation excess runoff, infiltration excess runoff, and base flow are evaluated separately.

Soil Heat conduction, water flow due to gravity and suction, freezing and thawing of soil water and root uptake of soil water are considered.

3.4   Boundary conditions

The boundary conditions required are land-cover type, soil type, leaf area index (LAI), soil albedo for visible and near-IR wavelength bands, mean surface slope, and the standard deviation of surface height. Most of them are generated from the ISLSCP Initiative I dataset, while the land-cover type is based on USGS GLCC and the standard deviation of surface height is based on USGS GTOPO30. The LAI should be prescribed by a monthly dataset, while the others are temporary constant.

4 River routing model

4.1 General features

The river routing model transports runoff water from the land-surface model to the ocean model at river mouths. The scheme is based on Miller et al. (1994), which prognose river water storage in each grid box. A globally uniform and temporary constant river flow speed of 0.3 m/s is used for simplicity. The flow of glacier (the snow amount exceeding a certain critical value is treated as glacier in the land-surface model) is also treated in this model, though the freezing and thawing of river water is not considered.

4.2 River routing data and resolution

In HI, the river routing dataset used is TRIP (Total Runoff Integrating Pathways; Oki and Sud, 1998). It specifies river flow direction as one of the 8 directions (N, NE, E, SE, S, SW, W, NW) at each grid box. The resolution of the model and the routing dataset is 0.5° in longitude and latitude. In MID, the resolution of the model is the same as that of atmospheric model, that is, T42 (∼2.8125°). The river flow direction dataset, similar in structure to TRIP, is the one developed by Dr. Shinjiro Kanae (personal communication). The time step is 3 hours for both HI and MID.

4.3 Treatment of inland depression

In the TRIP dataset, there are some inland points which have no outlets (inland depression). In HI, which uses TRIP, since evaporation of river water or infiltration of river water into soil is not considered, river water tends to be accumulated at those points. As a temporary expedient to avoid this accumulation, the river water in the inland depression points is sprinkled over surrounding grids. There is no inland depression in MID.

5　Ocean model

The ocean general circulation model used herein is CCSR Ocean Component Model (COCO) version 3.4. More detailed description of COCO can be found in Hasumi (2000).

5.1　General features

The basic equations of COCO is the primitive equations on a sphere, where the Boussinesq and hydrostatic approximations are adopted. The model explicitly represents the sea surface elevation. The vertical coordinate of the model is a hybrid of σ (normalized depth) and z (geopotential height): the former is applied between the sea surface and a fixed level in the upper ocean, and the latter below. The σ-coordinate is introduced in order to avoid disappearance of the top level. The model is formulated horizontally on the spherical coordinate system, and the rotation of the model grid system is available to avoid the coordinate convergence in the Arctic Ocean.

In solving the momentum equations, the horizontal velocity is decomposed into the barotropic mode (vertically integrated velocity) and the baroclinic mode (deviation from the vertical mean) in order to take a separate care for high-speed external gravity waves. A shorter time step is applied for the barotropic mode equations than for the remaining ones in numerical time-integration.

5.2　Discretization

The model equations are finite-differenced in both time and space. The grid spacing and the time step are fixed in time.

The model's prognostic variables are arranged horizontally on the Arakawa B staggard grid system. Coast lines are defined by the lines connecting velocity points. The partial step formulation (Adcroft et al., 1997) is applied for bottom topography representation, which allows to set the depth of the sea floor irrespective of the model vertical grid system.

Numerical time integration of the model's prognostic equations other than for the barotropic mode are basically achieved by the leap-frog and Euler-backward schemes: nine steps of the latter is applied after every ninety steps of the former, and one step of the Euler-forward scheme is used after the application of the Euler-backward scheme to prepare the values of the variables at two time levels. The tracer advection term is, however, integrated by use of the Euler-forward scheme, as an upstream-weighted algorithm is adopted. The horizontal diffusion and viscosity terms are also integrated by the Euler-forward scheme, while

the vertical diffusion and viscosity terms are integrated implicitly in time. A semi-implicit treatment is applied for the Coriolis term. For the barotropic mode equations, only the Euler-backward scheme is used as proposed by Killworth et al. (1991).

5.3   Model geometry and resolution

HI-resolution   The model spherical coordinate system is rotated so that the singular points of the coordinate are located on land. The north pole of the model coordinate system is shifted at 50°W, 77°N on Greenland. The horizontal resolution is 0.28125° zonally and 0.1875° meridionally, both in the rotated coordinate system. There are 47 vertical levels, excluding the bottom boundary layer, and 8 of which are within the σ-coordinate. The vertical grid spacing varies with depth, whose values are 2.5, 2.5, 3, 4, 5, 6, 7, 8, 10, 12, 14, 16, 18, 20, 25, 30, 35, 40, 50, 60, 80, 100, 120, 140, 160, 180, 200, 200, 200, 200, 200, 200, 200, 200, 200, 200, 200, 200, 200, 200, 200, 250, 250, 250, 250, 250, and 250 m, from the top to the bottom. Note that the values for the σ-coordinate region are under the zero sea level elevation. The time step of the model integration is 3 seconds for the barotropic mode equations and 3 minutes for the others.

The model bathymetry is generated from a widely used 2-minute resolution bathymetry data (ETOPO2). The depths of the ocean floor are first interpolated on the model grids, and then are spatially smoothed at high latitudes. The model geometry in the rotated grid system is shown in Figure 2. Most of the narrow straits connecting major basins and inland seas are naturally resolved at the current resolution. However, the Straits of Gibraltar is artificially widened. The depth of the Strait of Gibraltar is set at 668 m (23rd level).

MID-resolution   The model coordinate system coincides with the geographical spherical coordinate system. The zonal resolution is 1.40625° (= 360/256). The meridional resolution is about 0.56° at latitudes lower than 8°, 1.4° at latitudes higher than 65°, and smoothly changes in between. There are 43 vertical levels, excluding the bottom boundary layer, and 8 of which are within the σ-coordinate. The vertical grid spacing varies with depth, whose values are 5, 5, 5, 5, 5, 5, 7.5, 7.5, 10, 10, 10, 10, 15, 20, 25, 25, 30, 50, 75, 75, 100, 100, 150, 150, 150, 150, 200, 250, 250, 250, 250, 250, 250, 250, 250, 250, 250, 250, 250, 250, 250, 250, 250 m, from the top to the bottom. Note that the values for the σ-coordinate region are under the zero sea level elevation. The time step of the model integration is 30 seconds for the barotropic mode equations and 20 minutes for the others. Sea surface elevation, tracers, and velocity components are filtered in the zonal direction in the Arctic Ocean to use a time
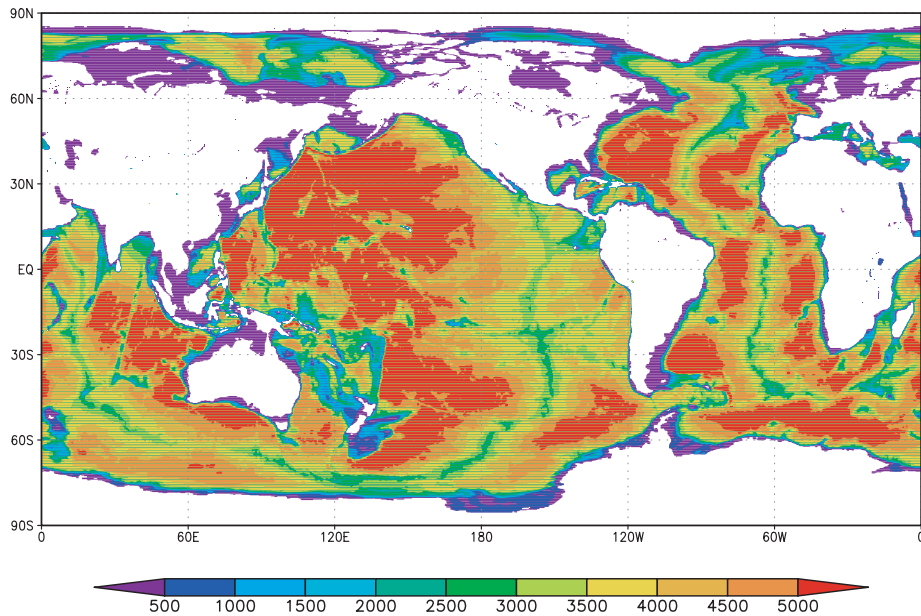
Figure 2: Model ocean bathymetry for HI in the rotated coordinate system.

step longer than the limit of the CFL condition in the Arctic Ocean. The filtering is done by repeated operation of the simplest symmetric finit impulse response filter, where the filtered value at a certain grid is obtained by the weighted average of the value at that grid and two adjacent grids with the weight of 2 for the central grid and 1 for the adjacent grids. Care is taken to conserve water volume and tracers.

The model bathymetry is generated from a widely used 5-minute resolution bathymetry data (ETOPO5). The depths of the ocean floor are first interpolated on the model grids, and then are spatially smoothed. The model geometry in the rotated grid system is shown in Figure 3. The Bering Strait is represented by a two-grid gap, which means there is only one velocity grid point at the strait. The water pathway through the Canadian Archipelago is also represented by artificially excavating a channel. The Mediterranean, Black, Caspian, and Red Seas and the Hudson Bay are represented as isolated basins. At the straits connecting these basins with the adjacent seas and oceans, sea surface elevation and tracers are artificially exchanged by two-way linear damping. The time constant of the damping is 100 days. The depth to which the damping is applied is 1650 m for the Strait of Gibraltar and 45 m for the other straits.
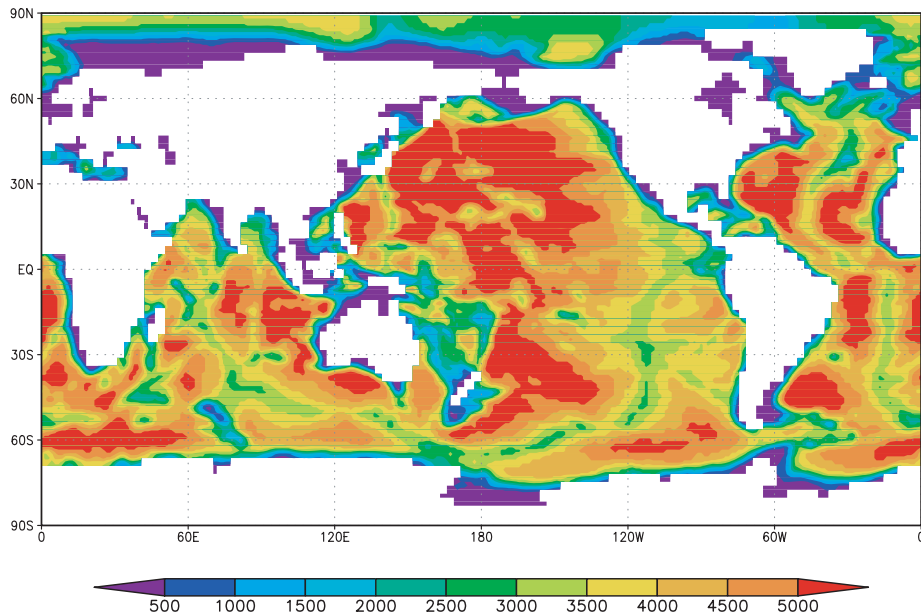
Figure 3: Model ocean bathymetry for MID.

5.4 Numerical algorithm

Barotropic mode equations The barotropic mode equations are made up of the vertically integrated momentum equations and the vertically integrated continuity equation. The formulation follows the method of Killworth et al. (1991). When the barotropic velocity components are combined with the baroclinic ones, an average over two baroclinic time steps is taken in order to satisfy the continuity equation, as indicated by Dukowicz and Smith (1994). In order to eliminate checker-board noise in the sea surface elevation field, weak horizontal diffusion is applied to sea surface elevation, with a care to conserve tracer quantities in the σ-coordinate region. The coefficient for the diffusion is 10 m^2/s for both HI and MID.

Momentum advection The model employs the momentum advection algorithm of Ishizaki and Motoi (1999) for HI, which is a pseudo-enstrophy preserving scheme with a consideration for up-/down-sloping advection. The momentum advection algorithm for MID is the second-order, energy-preserving one.

Tracer advection The model's tracer advection is based on the uniformly third-order polynomial interpolation algorithm (UTOPIA; Leonard et al., 1993). In its application to the model, however, the horizontal dimensions and the vertical dimension are separately

dealt with, so the vertical algorithm reduces to the quadratic upstream interpolation for convective kinematics with estimated streaming terms (QUICKEST; Leonard, 1979). The neglected vertical-horizontal cross term is generally small for hydrostatic models where the grid aspect ratio (vertical to horizontal) is much smaller than unity.

In the horizontal application of UTOPIA, the flux-integral method (Leonard et al. 1994) is used to guarantee the tracer quantity conservation. A flux limiter is required for numerical stability of QUICKEST and UTOPIA. There are single-dimensional flux limiters (e.g., Leonard, 1991) and multi-dimensional ones. The former has an advantage in terms of positivity preservation, while the latter has an advantage in terms of shape preservation, relative to the other. A single-dimensional one is adopted herein, as the multidimensional ones devised by Leonard et al. (1993) resulted in a problem where there is a strong cross-gradient current and its orientation is diagonal to the horizontal grid. Such a feature is often observed in the bottom boundary layer.

5.5 Physical parameterization

Vertical convection Since the hydrostacy is assumed, the vertical convection process should be appropriately parameterized to remove unstable vertical stratification. The way adopted here is the simplest convective adjustment, where a statically unstable water column is homogenized instantaneously.

Vertical mixing The vertical mixing of momentum and tracers is represented by a harmonic form. The diffusion and viscosity coefficients are calculated by the parameterization of Noh and Kim (1999), which is based on the level 2.5 turbulence closure of Mellor and Yamada (1982). The formulation is slightly modified to include dependence of the turbulent Prandtl number on the turbulent Richardson number:

$$Pr = Pr_0 + Pr_1 Ri, \tag{9}$$

where Pr is the turbulent Prandtl number, Pr_0 is its value at the neutral stability, Ri is the turbulent Richardson number, and Pr_1 is the parameter determining the dependence on Ri. Pr_0 is taken to be 0.8 as suggested by many experimental studies. Pr_1 is taken to be 7, following Kondo et al. (1978). An upper bound is imposed on Pr, which is set to 20. The value of the parameter α, which determines the model's behavior at high stability, is taken to be 3. Other model parameters are the same as given by Noh and Kim (1999).

As background diffusivity, a minimum value is prescribed for each level. The background viscosity coefficient is 1.0×10^{-4} m^2/s at all the levels. The background diffusion coefficient

varies with depth, from 0.1×10^{-4} m^2/s for the top to 3.0×10^{-4} m^2/s for the deepest model level. This vertical profile is suggested by Tsujino et al. (2000) to simulate the Pacific deep overturning circulation with sufficient intensity. Latitudinal dependence is assumed for the background vertical diffusivity. Gregg et al. (2003) suggest that the dissipation rate at low latitudes is significantly reduced compared with that for the same internal wave characteristics at higher latitudes. When it is referenced to the value derived from the Garret and Munk's (1975) internal wave spectrum at 30°, the factor to be multiplied by is modeled by them as

$$\frac{f \cosh^{-1}(N/f)}{f_{30°} \cosh^{-1}(N_0/f_{30°})}, \tag{10}$$

where f is the Coriolis parameter, $f_{30°}$ is its value at 30°, N is the buoyancy frequency, and N_0 ($= 5.24 \times 10^{-3}$ /s) is the reference stratification assumed in the model of Garret and Munk (1975). This functional form is applied directly to the background diffusivity, not to the dissipation rate, in our model. Since N is not known *a priori*, it is taken to be the same as N_0 for the current application.

Lateral mixing of momentum The Smagorinsky's (1963) biharmonic viscosity is applied for the lateral momentum mixing in HI. Its coefficient is dependent on the grid width and the strain rate, and is controlled by a single nondimensional parameter whose value is taken to be 4. The harmonic viscosity is used in MID with the coefficient value of 3.0×10^4 cm^2/s. At latitudes higher than 60°, the coefficient is linearly reduced to zero with increasing latutide.

Lateral mixing of tracer The constant coefficient biharmonic diffusion is applied as the background in HI: the value of the coefficient is 1.0×10^9 m^4/s. Harmonic isopycnal diffusion is also applied with the coefficient value of 1.0×10^3 m^2/s.

Since the HI-resolution model's horizontal grid spacing is not fine enough to resolve mesoscale eddies at high latitudes, it is necessary to introduce some parameterization for eddy-induced transport of tracers. The harmonic horizontal diffusion of isopycnal layer thickness (Gent et al., 1995) is applied at high latitudes. The value of the thickness diffusion coefficient is 7.0×10^2 m^2/s for latitudes higher than 50°, is 0 for latitudes lower than 40°, and linearly changes in between.

For MID, the harmonic horizontal diffusion, the harmonic isopycnal diffusion, and the harmonic hirozontal diffusion of isopycnal layer thickness are applied, whose coefficients are 1.0×10^2 m^2/s, 1.0×10^3 m^2/s, and 7.0×10^2 m^2/s, respectively.

Bottom boundary layer Down-sloping flow of dense water, which is a crucial process for the deep overturning circulation, is not naturally represented at the current model resolution. The bottom boundary layer parameterization of Nakano and Suginohara (2002) is incorporated into the model to represent it. In this parameterization, a bottom boundary layer of fixed depth is assumed, entrainment at the top of the layer is represented by enhanced vertical diffusivity, and the ageostrophic effect of eddies is represented by the bottom Rayleigh drag. The layer thickness is 80 m for HI and 100 m for MID, the vertical diffusion and viscosity coefficients at the top of the layer are 5.0×10^{-4} m^2/s and 1.0×10^{-4} m^2/s, respectively. The Rayleigh drag coefficient is taken to be the same as the Coriolis parameter above 2000 m and zero below. Horizontal viscosity is considered within the layer, whose formulation and coefficient are the same as for the upper layers. No horizontal diffusion of tracers is applied. The bottom boundary layer is applied only at high latitudes, to the north of 49°N and to the south of 54°S, following Nakano and Suginohara (2002).

Vertical penetration of shortwave radiative flux The shortwave radiative flux absorbed by the ocean penetrates into deeper levels. The attenuation of the shortwave flux in the ocean is calculated by following the formulation of Rosati and Miyakoda (1988).

6 Sea ice model

6.1 General features

Sea ice is treated as a two-dimensional continuum. In each horizontal grid, concentration, mean thickness (over the ice-covered portion), and horizontal velocity components are predicted. Sea ice concentration and thickness change due to thermodynamic growth/decay, advection, and mechanical deformation of ice floes.

6.2 Model resolution

The horizontal resolution of the sea ice model is taken to be the same as that of the ocean model. The time step of the integration is also the same as for the ocean model (for other than barotropic mode equations). The time splitting method is used in solving the momentum equation with the elastic-viscous-plastic rheology (described later), where the time step is chosen to be 3 seconds for HI and 30 seconds for MID.

6.3 Thickness category representation

This sea ice model is classified as two-category in terms of the representation of subgrid-scale sea ice thickness distribution. In typical two-category models, a minimum value is prescribed for mean thickness, and this minimum thickness is used as a parameter distinguishing thin and thick ice. Mechanical characteristics are very different between thin ice (such as pancakes) and thick ice (such as multi-year ice and ridged ice). In the early stage of new ice formation, sea ice is often formed as frazil, which does not exhibit such a solid form as an ice floe. Even after sea ice takes a solid form such as a pancake, collision of thin ice floes often results in rafting, not ridging. From the dynamical perspective, therefore, it is reasonable to treat ice thinner than a certain threshold categorically as identical to open water. In the model, newly formed thin ice is instantaneously converted into ice of the minimum or larger thickness. The minimum thickness in this model is 0.1 m.

6.4 Thermodynamics

The simplest zero-layer thermodynamics (Semtner, 1976) is assumed in the sea ice model, where the heat content of sea ice is neglected and only the latent heat of melt is taken into account in the heat budget consideration. Snow cover on sea ice is treated likewise.

The vertical heat transfer within sea ice is calculated by

$$F_I = k_I k_s \frac{T_o - T_s}{k_I h_s + k_s h_I} \tag{11}$$

where F_I is the vertical heat flux through sea ice (positive upward), h_I is the sea ice thickness, h_s is the snow cover thickness, and k_I (= 2.04 W/m/K) and k_s (= 0.31 W/m/K) are the heat conductivity of sea ice and snow, respectively. T_o is the ice bottom temperature, which coincides with the freezing point of the seawater below, and T_s is the temperature at the air-ice (snow when exists) interface. The freezing point of seawater, T_f, is given by a function of salinity as $T_f = -0.0543S$, where T_f is measured by the degree Celsius and the unit of salinity S is the practical salinity unit (psu).

The air-ice/snow interface temperature is determined by the heat balance at the interface. If the diagnosed air-ice/snow interface temperature goes beyond the freezing point of pure water, the temperature is reset at the freezing point and the heat flux imbalance is consumed by melting ice/snow.

Sea ice exists only when and where the ocean model's top level is at the freezing point. If the seawater temperature under sea ice exceeds the freezing point in the course of the model integration, the sea ice amount is reduced until the seawater temperature settles down at the freezing point.

When open water of a partially ice-covered grid is cooled, newly formed thin ice eventually reduces the mean sea ice thickness. This process can be represented by setting the predicted sea ice concentration at unity. In a two-category model, however, such a treatment could conflict with the interpretation of thin ice in the model. Still, some increase in concentration should happen under cooling, even by reducing mean thickness. From this standpoint, it should be parameterized to what degree concentration should increase under the cooling of open water. When open water of a partially ice-covered grid is warmed, on the other hand, absorbed water is to be consumed to melt sea ice both from the ice edge (reduces the concentration) and from the ice bottom (reduced the thickness): the latter due to the heat transfer within the sea surface mixed layer. Thus, in this case, the partitioning between the lateral and basal melting should be parameterized. These are parameterized by following the method of Mellor and Kantha (1989), with the same parameter values as described therein.

6.5 Freshwater budget

Sea ice is assumed to contain constant salinity, which is taken to be 5 psu in the current modeling. Melt ponds are not taken into consideration in the model, so the melt water immediately runs off into the ocean.

The level of the snow-ice interface relative to the sea surface is determined by the density of snow and ice. When it goes below the sea surface, snow is converted to sea ice until the interface level coincides with the sea surface (snow-ice formation). In this process, salinity is added to the newly formed snow-ice to guarantee the salt conservation. It is more physically reasonable to reduce the salinity of sea ice, but such a treatment requires to deal with the sea ice salinity as a prognostic variable.

6.6 Dynamics

Sea ice concentration and mean thickness are advected by the sea ice horizontal velocity with conserving the volume. The advection term is numerically integrated by using the weighted upstream algorithm, which is a mixture of the upstream and centered-in-space algorithms. Harmonic and biharmonic diffusion is taken into account for the sake of numerical stability, whose coefficients are 1.0×10^2 m^2/s and 1.0×10^8 m^4/s, respectively, for HI. The coefficients are 1.0×10^4 m^2/s and 1.0×10^{12} m^4/s for MID.

The momentum equation of sea ice is composed of the advection term, the Coriolis term, the acceleration term due to sloping of the sea surface, the internal stress term, and the external forcing term (e.g., Hibler, 1979). The external forcing is the sum of wind stress and ice-ocean drag. A quadratic form is assumed for the ice-ocean drag term, as in Hibler (1979), and the drag coefficient is taken to be 0.005. Sea ice concentration is not allowed to exceed unity. When ice volume convergence occurs in a compactly packed grid, ice thickness increases without changing concentration. This represents the sea ice ridging process. The mechanical resistance to the ridging is represented by the internal stress term in the momentum equation, and is formulated by the elastic-viscous-plastic rheology of Hunke and Dukowicz (1997). The parameters for the internal stress are also taken from Hunke and Dukowicz (1997), except for the parameter representing the strength of the ice of the unit thickness and concentration (P^* in their paper), which is taken to be 2.0×10^2 N/m.

6.7 Lead parameterization

Leads are generally underestimated in large-scale models due, for example, to the lack of short-term forcing variations. Observations indicate that 1–2 % of open water exists even for the wintertime central Arctic, and the air-sea heat exchange through such leads accounts for more than half of the wintertime basin-scale heat budget (e.g., Maykut, 1982).

In this model, lead formation is parameterized by imposing a maximum value for sea ice concentration. The maximum concentration depends on thickness: it is 0.95 for the

minimum thickness, is unity for ice thicker than 6 m, and linearly changes in between.

6.8   Air-sea fluxes

The sea ice model also functions as the coupled model's air-sea interface, and the fluxes exchanged between the atmosphere and the ocean are calculated herein.

Heat flux   The latent and sensible heat fluxes are calculated by using bulk formulae, which are based on those of Louis (1979) with modifications by Uno et al. (1995). Roughness of open ocean is determined by the method of Miller et al. (1992), and that for snow and ice covered surface is prescribed at 1.0×10^{-3} m and 2.0×10^{-3} m, respectively. The fluxes are calculated separately for open water and ice/snow-covered surface at each horizontal atmosphere-sea ice coupler grid (see section 1.1 for what the "atmosphere-sea ice coupler" means). The upward longwave radiative flux is calculated by the Stefan-Boltzmann's fourth power low of the surface temperature, with the emissivity of 0.95. This calculation is also made separately for open water and ice/snow-covered surface. The surface albedo of open water depends on the solar zenith angle. It is calculated by a three-coeffcient polynomial fit of the Payne's (1972) data. Albedo of the bare ice surface is fixed at 0.5. Albedo of the snow-covered surface depends on temperature by taking into consideration the existence of partial snow-cover at a relatively high temperature. It is 0.9 for temperature lower than 15°C, is 0.7 for 0°C, and changes linearly in between for HI. For MID, it is 0.85 for temperature lower than 15°C, is 0.65 for 0°C, and changes linearly in between.

Together with the downward shortwave and longwave radiative fluxes, which are calculated by the atmospheric model, the air-sea/ice heat flux is determined. For the ice/snow surface, the surface temperature is also determined in this procedure. Penetration of the shortwave radiative flux into snow or sea ice is not taken into account.

Freshwater flux   The freshwater flux due to evaporation or sublimation is determined in consistent with the latent heat flux. When sea ice sublimates, the contained salt is drained into the ocean in order to guarantee the salt conservation. Precipitation calculated by the atmospheric model is passed to the sea ice model. Snowfall accumulates on sea ice surface, while rainfall is directly added to seawater below. When snow falls on open water, the corresponding latent heat of melt is taken away from the top level. Liquid and solid water runs off from the river model. Liquid water runoff is added to rainfall, and solid water runoff is added to snowfall.

Momentum flux The wind stress is also calculated by use of the bulk formula of Louis (1979), with modifications by Uno et al. (1995) and the open water surface roughness formualtion of Miller et al. (1992). Surface roughness for snow and ice is 1.0×10^2 m and 2.0×10^2 m, respectively. The ice-ocean drag stress, obtained as a result of the sea ice dynamics calculation, is added to the wind stress for open ocean with the weight of the sea ice concentration and passed to the ocean.

The wind stress τ is filtered in time when it is passed to sea ice or the ocean. The filtered value $\tilde{\tau}$ is calculated by

$$\tilde{\tau}(t) = \frac{1}{T} \int_{-\infty}^{t} \tau(t') e^{(t'-t)/T} dt', \tag{12}$$

where t is time and T is the time-scale of the filtering, which is chosen to be 1 day.

References

Adcroft, A., C. Hill, and J. Marshall, 1997: Representation of topography by shaved cells in a height coordinate ocean model, *Mon. Wea. Rev.*, **125**, 2293-2315.

Arakawa, A., and W. H. Schubert, 1974: Interactions of cumulus cloud ensemble with the large-scale environment. Part I, *J. Atmos. Sci.*, **31**, 671-701.

Arakawa A., and M. J. Suarez, 1983: Vertical differencing of the primitive equations in sigma coordinates, *Mon. Wea. Rev.*, **111**, 34-45.

Ball, J. T., 1998: An analysis of stomatal conductance, PhD dissertation, Stanford University, 89pp.

Berry, E. X., 1967: Cloud droplet growth by collection. *J. Atmos. Sci.*, **24**, 688-701.

Beven, K. J., and M. J. Kirkby, 1979: A physically based, variable contributing area model of basin hydrology, *Hydrol. Sci. Bull.*, **24**, 43-69.

Carpenter, R. L., Jr., K. K. Drogemeier, P. R. Woodward, and C. E. Hane, 1990: Application of the piecewise parabolic method to meteorological modelling, *Mon. Wea. Rev.*, **118**, 586-612.

Colella, P., and P. R. Woodward, 1984: The Piecewise Parabolic Method (PPM) for Gas-Dynamical Simulations, *J. Comput. Phys.*, **54**, 174-201.

d'Almeida, G. A., P. Koepke, and E. P. Shettle, 1991: Atmospheric Aerosols: Global Climatology and Radiative Characteristics, Ed. A. Deepak, 561 pp.

Dukowicz, J. K., and R. D. Smith, 1994: Implicit free-surface method for the Bryan-Cox-Semtner ocean model, *J. Geophys. Res.*, **99**, 7991-8014.

Emori, S., T. Nozawa, A. Numaguti and I. Uno, 2001: Importance of cumulus parameterization for precipitation simulation over East Asia in June, *J. Meteorol. Soc. Japan*, **79**, 939-947.

Farquhar, G. D., S. von Caimmerer and J. A. Berry, 1980: A biochemical model of photosynthetic CO_2 fixation in leaves of C_3 species, *Planta*, **149**, 78-90.

Garret, C. J. R., and W. H. Munk, 1975: Space-time scales of internal waves: A progress report, *J. Geophys. Res.*, **80**, 291-297.

Geleyn, J. F., and A. Hollingsworth, 1979: An economical analytical method for the computation of the interaction between scattering and line absorption of radiation, *Contrib. Atmos. Phys.*, **52**, 1-16.

Gent, P. R., J. Willebrand, T. J. McDougall, and J. C. McWilliams, 1995: Parameterizing eddy-induced tracer transports in ocean circulation models, *J. Phys. Oceanogr.*, **25**, 463-474.

Gregg, M. C., T. B. Sanford, and D. P. Winkel, 2003: Reduced mixing from the breaking of internal waves in equatorial waters, *Nature*, **422**, 513-515.

Gregory, D., R. Kershaw and P. M. Inness, 1997: Parametrization of momentum transport by convection. II: Tests in single-column and general circulation models, *Q. J. R. Meteorol. Soc.*, **123**, 1153-1183.

Hasumi, H., 2000: CCSR Ocean Component Model (COCO) Version 2.1, *CCSR Report*, **13**, 68pp.

Hibler, W. D., III, 1979: A dynamic thermodynamic sea ice model, *J. Phys. Oceanogr.*, **9**, 815-846.

Hobbs, P. V., J. S. Reid, R. A. Kotchenruther, R. J. Ferek and R. Weiss, 1997: Direct radiative forcing by smoke from biomass burning, *Science*, **275**, 1776-1778.

Holtslag, A. A. M., and B. Boville, 1993: Local versus nonlocal boundary-layer diffusion in a global climate model, *J. Climate*, **6**, 1825-1842.

Hunke, E. C., and J. K. Dukowicz, 1997: An elastic-viscous-plastic model for sea ice dynamics, *J. Phys. Oceanogr.*, **27**, 1849-1867.

Ishizaki, H., and T. Motoi, 1999: Reevaluation of the Takano-Oonishi scheme for momentum advection on bottom relief in ocean models, *J. Atmos. Oceanic Tech.*, **16**, 1994-2010.

Killworth, P. D., D. Stainforth, D. J. Webb, and S. M. Paterson, 1991: The development of a free-surface Bryan-Cox-Semtner ocean model, *J. Phys. Oceanogr.*, **21**, 1333-1348.

Leonard, B. P., 1979: A stable and accurate convective modelling procedure based on quadratic upstream interpolation, *Comp. Methods Appl. Mech. Eng.*, **19**, 59-98.

Leonard, B. P., M. K. MacVean, and A. P. Lock, 1993: Positivity-preserving numerical schemes for multidimensional advection, NASA Tech. Memo. 106055, ICOMP-93-05, 62pp.

Leonard, B. P., M. K. MacVean, and A. P. Lock, 1994: The flux-integral method for multidimensional convection and diffusion, NASA Tech. Memo. 106679, ICOMP-94-13, 29pp.

Le Treut, H., and Z.-X. Li, 1991: Sensitivity of an atmospheric general circulation model to prescribed SST changes: feedback effects associated with the simulation of cloud optical properties, *Climate Dynamics*, **5**, 175-187.

Lin, S.-J., and R. B. Rood, 1996: Multidimensional flux-form semi-Lagrangian transport schemes, *Mon. Wea. Rev.*, **124**, 2046-2070.

Lin, S.-J., W. C. Chao, Y. C. Sud and K. Walker, 1994: A class of the van Leer-type transport schemes and its application to the moisture transport in a general circulation model, *Mon. Wea. Rev.*, **122**, 1575-1593.

Louis, J., 1979: A parametric model of vertical eddy fluxes in the atmosphere, *Bound.-Layer Meteor.*, **17**, 187-202.

Maykut, G. A., 1982: Large-scale heat exchange and ice production in the Central Arctic, *J. Geophys. Res.*, **87**, 7971-7984.

Mellor, G. L., and T. Yamada, 1982: Development of a turbulence closure model for geostrophic fluid problems, *Rev. Geophys.*, **20**, 851-875.

Mellor, G. L., and L. Kantha, 1989: An ice-ocean coupled model, *J. Geophys. Res.*, **94**, 10,937-10,954.

Mesinger, F., and A. Arakawa, 1976: Numerical methods used in atmospheric models, GARP Publications Series 17, WMO–ICSU Joint Organising Committee, 64pp.

Miller. M. J., A. C. M. Beljaars, and T. N. Palmer, 1992: The sensitivity of the ECMWF model to the parameterization of evaporation from the tropical oceans, *J. Climate*, **5**, 418-434.

Nakajima, T., M. Tsukamoto, Y. Tsushima, A. Numaguti and T. Kimura, 2000: Modelling of the radiative process in an atmospheric general circulation model, *Appl. Opt.*, **39**, 4869-4878.

Nakano, H., and N. Suginohara, 2002: Effects of bottom boundary layer parameterization on reproducing deep and bottom waters in a World Ocean model, *J. Phys. Oceanogr.*, **32**, 1209-1227.

Noh, Y., and H.-J. Kim, 1999: Simulations of temperature and turbulence structure of the oceanic boundary layer with the improved near-surface process, *J. Geophys. Res.*, **104**, 15,621-15,634.

Numaguti, A., M. Takahashi, T. Nakajima and A. Sumi, 1997: Description of CCSR/NIES Atmospheric General Circulation Model, *CGER's Supercomputer Monograph Report, Center for Global Environmental Reserch, National Institute for Environmental Studies*, No.3, 1-48.

Oki, T., and Y. C. Sud, 1998: Design of total runoff integrating pathways (TRIP) - a global river channel network, *Earth Interactions*, **2**.

Pan, D.-M., and D. A. Randall, 1998: A cumulus parameterization with a prognostic closure, *Q. J. R. Meteorol. Soc.*, **124**, 949-981.

Payne, R. E., 1972: Albedo of the sea surface, *J. Atmos. Sci,*, *29*, 959-970.

Rosati and Miyakoda, 1988: A general circulation model for upper ocean simulation, *J. Phys. Oceanogr.* *18*, 1601-1626.

Semtner,A. J., Jr., 1976: A model for the thermodynamic growth of sea ice in numerical investigations of climate, *J. Phys. Oceanogr.*, **6**, 379-389.

Shibata, K., and A. Uchiyama, 1992: Accuracy of the delta-four-stream approximation in inhomogeneous scattering atmosphere, *J. Meteorol. Soc. Japan*, **70**, 1097-1109.

Smagorinsky, J., 1963: General circulation experiments with the primitive equations, *Mon. Wea. Rev.*, **91**, 99-164.

Smith, R. N. B., 1990: A scheme for predicting layer clouds and their water content in a general circulation model, *Q. J. R. Meterol. Soc.*, **116**, 435-460.

Takata, K., T. Watanabe and S. Emori, 2003: Development of the minimal advanced treatments of surface interaction and runoff, *Global and Planetary Change*, **38**, 209-222.

Takemura, T., H. Okamoto, Y. Maruyama, A. Numaguti, A. Higurashi and T. Nakajima, 2000: Global three-dimensional simulation of aerosol optical thickness distribution of various origins, *J. Geophys. Res.*, **105**, 17,853-17,873.

Takemura, T., T. Nakajima, O. Dubovik, B. N. Holben and S. Kinne, 2002: Single-scattering albedo and radiative forcing of various aerosol species with a global three-dimensional model, *J. Climate*, **15**, 333-352.

Tang, I. N., and H. R. Munkelwitz, 1994: Water activities, densities, and refractive indices of aqueous sulfates and sodium nitrate droplets of atmospheric importance, *J. Geophys. Res.*, **99**, 18,801-18,808.

Tsujino, H., H. Hasumi and N. Suginohara, 2000: Deep Pacific circulation controlled by vertical diffusivity at the lower thermocline depths, *J. Phys. Oceanogr.*, **30**, 2853-2865.

Uno, I., X.-M. Cai, D. G. Steyn, and S. Emori, 1995 A simple extension of the Louis method for rough surface layer modelling, *Bound.-Layer Meteor.*, **76**, 395-409.

Watanabe, T., 1994: Bulk parameterization for a vegetated surface and its application to a simulation of nocturnal drainage flow, *Boundary-Layer Meteorol.*, **70**, 13-35.

WCP-55, 1983: Reports of the experts meeting on aerosols and their climatic effects, Eds. A. Deepak and H. E. Gerber, World Meteorological Organization, 107 pp.

Wiscombe, W. J., and S. G. Warren, 1980: A model for the spectral albedo of snow: I. Pure snow, *J. Atmos. Sci.*, **37**, 2712-2733.